Journal of Alloys and Compounds 1036 (2025) 182130

Contents lists available at ScienceDirect

Journal of Alloys and Compounds

journal homepage: www.elsevier.com/locate/jalcom

Unveiling the micro-mechanism of superior dehydrogenation in γ-MgH_2: Insights into electronic structure of H–Mg bond

Wenfeng Fu [a,b], Man Shu [a,b], Yuxuan Liu [a,b], Jien Shi [a,b], Zhuoran Xu [a,b], Tongao Yao [a,b], Xinyuan Liu [a,b], Shuai Dong [a,b], Zhengyang Gao [a,b], Weijie Yang [a,b,*]

[a] Department of Power Engineering, School of Energy, Power and Mechanical Engineering, North China Electric Power University, Baoding 071003, China
[b] Hebei Key Laboratory of Energy Storage and Integrated Energy Systems, North China Electric Power University, Baoding, Hebei 071003, China

ARTICLE INFO

Keywords:
Hydrogen storage, γ-MgH_2, Density functional theory, Electronic structure analysis, Ionicity index

ABSTRACT

Mechanical ball milling yields a metastable γ-MgH_2 phase with a lower dehydrogenation temperature than conventional MgH_2, offering a potential solution for solid-state hydrogen storage, but its unclear microscopic mechanism hinders further application. To address this challenge, we employed density functional theory calculations to unveil the micro-mechanism of superior dehydrogenation of γ-MgH_2 from the insights of H–Mg binding electric structures. *Ab initio* molecular dynamics simulations reveal that γ-MgH_2 can spontaneously undergo dehydrogenation at 373 K, which is consistent with previous experimental observations and outperforms the thermodynamically stable α-MgH_2 phase. Crystal orbital Hamilton population analysis indicates pronounced antibonding state occupation below the Fermi level, evidencing substantial weakening of H–Mg bonds and reducing its dehydrogenation temperature. Electron localization function results further confirm reduced bond localization, indicating weaker chemical bonding. Density of states analysis shows the presence of H-*s* states near the Fermi level, suggesting enhanced hydrogen mobility and favorable dehydrogenation kinetics. Furthermore, Bader charge analysis quantifies charge transfer and allows calculation of the ionicity index, establishing a clear correlation: systems with an ionicity index below 0.77 exhibit spontaneous dehydrogenation at low temperature. This study not only provides microscopic insight into the exceptional dehydrogenation performance of γ-MgH_2 but also proposes the ionicity index as a key descriptor for evaluating dehydrogenation ability in metal hydrides, offering a new strategy for designing high-performance hydrogen storage materials.

1. Introduction

As a clean and efficient energy carrier, hydrogen is playing an increasingly vital role in the transition toward sustainable energy systems by offering significant potential to reduce greenhouse gas emissions across transportation, energy, and industrial sectors [1–4]. Solid-state hydrogen storage is regarded as one of the most promising approaches owing to its high storage density and enhanced safety [5–7]. MgH_2 has a theoretical hydrogen storage capacity of up to 7.6 wt% and the highest energy density among reversible hydrides [8], which makes it a highly promising hydrogen storage material. However, the practical application of MgH_2 is hindered by its high thermal stability and sluggish hydrogen desorption kinetics [9]. Its relatively high hydride formation enthalpy (~75 kJ/mol) requires a dehydrogenation temperature above 300 °C, which severely restricts its practical use [10,11].

To improve the dehydrogenation performance of MgH_2, various strategies have been developed to lower its operating temperature. Carbon-based single-atom catalysts can reduce the dehydrogenation energy barrier by 0.51–2.22 eV [12–20]. Ti_3C_2 (MXene), obtained by etching Ti_3AlC_2, shows excellent catalytic activity [21–23]. Loading Cu nanoparticles onto MXene enables efficient photothermal synergistic catalysis [24,25]. Moreover, N-doped TiO_2 nanosheets coated with TiN nanoparticles integrate light absorption and thermocatalysis at the nanoscale [26–29]. Nanostructures and spatial nanoconfinement have been employed to regulate and optimize the hydrogen absorption/desorption kinetics and thermodynamics of MgH_2[30–35]. MgH_2 is doped with various metals such as Ni, Cu, Fe, Al, Co, and Ba, as well as alloyed with Li and Mg to form metal hydride composites or alloys with improved hydrogen storage properties [18,36–42], and ball milling treatment is applied during its preparation [43,44]. These strategies can

---

* Corresponding author at: Department of Power Engineering, School of Energy, Power and Mechanical Engineering, North China Electric Power University, Baoding 071003, China.
E-mail address: yangwj@ncepu.edu.cn (W. Yang).

https://doi.org/10.1016/j.jallcom.2025.182130
Received 12 May 2025; Received in revised form 3 July 2025; Accepted 7 July 2025

adjust and optimize the dehydrogenation kinetics of MgH_2.

Ball milling can reduce the dehydrogenation temperature of MgH_2 by approximately 100 °C. In an experimental study, Zhao et al. observed the formation of a γ-MgH_2 phase, distinct from the conventional α-MgH_2, during the ball milling process [45,46]. The presence of this phase facilitates dehydrogenation, making the milled material more prone to dehydrogenation. Moreover, ball milling is a straightforward and cost-effective mechanical processing method. γ-MgH_2 is a metastable phase of magnesium hydride. Compared to the commonly observed α-MgH_2 phase, γ-MgH_2 exhibits a significantly lower dehydrogenation temperature, which can be attributed to its unique crystal structure and the resulting special H–Mg bonding [47]. Although γ-MgH_2 is thermodynamically metastable, it remains kinetically stable under ambient pressure and can undergo dehydrogenation at temperatures below 300 °C, demonstrating considerable potential for hydrogen storage applications [46]. Therefore, investigating γ-MgH_2 is of great importance. Although the favorable dehydrogenation behavior of γ-MgH_2 has been well demonstrated at the macroscopic level, its underlying microscopic mechanisms remain poorly understood. A deeper understanding at the atomic and electronic structure level is urgently needed to guide the development of hydrogen storage materials with improved performance.

In recent years, density functional theory (DFT) calculations have been widely employed to investigate the microscopic mechanisms of hydrogen desorption in hydrogen storage materials, as well as to explore various chemical reactions and catalytic processes at the atomic level [48–53]. These studies have provided theoretical insights into atomic- and electronic-scale phenomena, such as the “burst effect” in MgH_2 and kinetic models of metal hydrides, offering valuable guidance for the design of advanced hydrogen storage materials [54,55]. Therefore, applying DFT to investigate the dehydrogenation mechanism of γ-MgH_2 is both meaningful and effective. The DFT approach enables a deeper understanding of the microscopic factors that drive the enhanced dehydrogenation properties of γ-MgH_2. Sander et al. employed DFT calculations to investigate the point defect kinetics of γ-MgH_2, revealing the influence of vacancies on its dehydrogenation behavior [56]. Kelkar et al. analyzed the effects of Al and Si doping on MgH_2, as well as the impact of high-pressure phases on its hydrogen absorption performance, through electronic structure analysis[57,58]. These studies suggest that DFT is a powerful tool for exploring the unique nature of H–Mg bonding in γ-MgH_2 at the electronic structure level. Therefore, DFT methods can be employed to investigate the unique characteristics of H–Mg bonding in γ-MgH_2 at the electronic structure level, aiming to uncover the microscopic mechanisms underlying its superior dehydrogenation behavior and to gain deeper insight into the factors that enhance its dehydrogenation performance.

In this work, first-principles calculations were employed to investigate the dehydrogenation behavior of γ-MgH_2 on different crystallographic surfaces. Based on previous studies, the (001), (100), (101), and (110) surfaces of MgH_2 are commonly studied due to their distinct structural features. The (110) surface is thermodynamically the most stable and is commonly used as a reference. Meanwhile, the (001), (100), and (101) surfaces exhibit higher atomic exposure, which facilitates hydrogen migration and makes them more susceptible to catalytic modification [54,59,60]. These surfaces are thus central to theoretical investigations of hydrogen storage and surface reaction mechanisms. Therefore, these four surfaces were selected to explore the origin of the superior dehydrogenation performance of γ-MgH_2. *Ab initio* molecular dynamics (AIMD) simulations were performed, and dehydrogenation phenomena were observed on the different surfaces, which correspond well with experimental findings. Subsequently, the radial distribution function (RDF) was calculated to analyze the local structural environment, followed by the evaluation of the root mean square displacement (RMSD) to quantify atomic mobility. To further analyze the bonding characteristics, the crystal orbital Hamilton population (COHP) method was used to evaluate the H–Mg bond strength during dehydrogenation [61,62]. The density of states (DOS) was computed to examine the electronic structure, and the electron localization function (ELF) was used to assess the impact of dehydrogenation on electron localization. Finally, Bader charge analysis was carried out to investigate the relationship between ionicity and dehydrogenation behavior on different surfaces. These results provide fundamental insights into the microscopic mechanisms underlying the excellent dehydrogenation performance of γ-MgH_2.

2. Experimental section

Density functional theory (DFT) calculations were performed using the Vienna *Ab initio* Simulation Package (VASP). The projector augmented wave (PAW) method was adopted, and the exchange-correlation interactions were treated using the Perdew–Burke–Ernzerhof (PBE) functional under the generalized gradient approximation (GGA) [63–65], which provides relatively accurate descriptions of hydrogen adsorption and desorption [66,67]. The PBE functional is widely used in hydrogen storage studies to evaluate H_2 adsorption and substrate interactions [13,14,54]. Given the non-magnetic nature of γ-MgH_2, spin polarization was omitted (ISPIN = 1). In all calculations, MgH_2 was treated as a semiconductor, and Gaussian smearing (ISMEAR = 0, SIGMA = 0.05 eV) was applied to ensure accurate COHP and DOS results. In order to accurately model the weak H–H interactions, which may influence the hydrogen desorption behavior observed in the simulations, we activated van der Waals corrections by setting IDVW = 12 [68]. A dipole correction was applied along the z-direction in all calculations.

To sample the dehydrogenation behavior of γ-MgH_2, AIMD simulations were conducted using the AIMD module implemented in the VASP code. To ensure accurate temperature control while avoiding the structural fluctuations associated with the isothermal–isobaric (NPT) ensemble and the lack of temperature regulation in the microcanonical (NVE) ensemble, AIMD simulations were carried out in the canonical (NVT) ensemble using the Nosé–Hoover thermostat. A time step of 1 fs was applied, and each model was simulated for 5 ps to eliminate non-equilibrium effects and capture thermally activated dehydrogenation and structural responses within a reasonable computational cost. The electronic self-consistent field (SCF) convergence criterion was set to 10^{-4} eV. It should be noted that this SCF criterion pertains specifically to the energy and force evaluations at each AIMD time step, and is distinct from the SCF settings typically used in static electronic structure calculations. The symmetry of the system was fully disabled to ensure accurate molecular dynamics sampling, and real-space projection was enabled to accelerate the calculations.

Due to the relatively large size of the simulation supercells, Brillouin zone sampling was performed using the Γ-point approximation with a $1 \times 1 \times 1$ k-point mesh. Both the initial and final temperatures of the simulations were set to 373 K. A plane-wave cutoff energy of 500 eV was used throughout the simulations.

After the AIMD simulations, post-processing analysis was conducted using the VMD software to calculate the RDFs of H–H distance, followed by the evaluation of the RMSDs [69].

The RDF characterizes the variation in local number density of particles as a function of distance from a reference particle, normalized by the average density. It offers insight into the structural arrangement of the system. The RDF between atom a and b is defined as:

$$g_{ab}(r) = \frac{\rho_{ab}(r)}{N_b/V} \tag{1}$$

The radial distribution function $g_{ab}(r)$ describes the probability of finding a particle of type b at a distance r from a reference particle of type a, relative to an ideal gas at the same density. Here, $\rho_{ab}(r)$ represents the local number density of b-type particles around an a-type particle at distance r. N_b is the total number of b-type particles in the system, and V denotes the total volume of the simulation cell.

The RMSD is a widely used metric to quantify the structural difference between two molecular conformations. The RMSD was computed using the following equation:

$$\mathrm{RMSD} = \sqrt{\frac{1}{N}\sum_{i=1}^{N}\left\|\mathbf{x}_i - \mathbf{y}_i\right\|^2} \tag{2}$$

In the formula, N represents the number of atom pairs being compared, x_i and y_i denote the three-dimensional coordinates of the i-th atom in the two structures respectively, and $|| \bullet ||$ represents the Euclidean distance. The meaning of the formula is that for each pair of corresponding atoms in the two structures, the squared distance between them is calculated, then the average of these squared distances is taken, and finally the square root of that average gives the overall deviation value.

Following the AIMD simulations, SCF calculations were carried out to analyze the electronic structure. A denser Monkhorst-Pack 4 × 4 × 1 *k*-point grid was used, along with increased precision settings to obtain accurate charge density and electrostatic potential distributions. Fig. S1 presents the results of the *k*-points test. A plane-wave cutoff energy of 450 eV was applied to describe the valence electrons. All calculations were spin-polarized, and the SCF total energy convergence criterion was set to 10^{-5} eV. The symmetry of the system was completely turned off to allow full electronic relaxation. Charge analysis was performed, and the ELF was computed to investigate the bonding characteristics.

To elucidate the bonding characteristics and charge transfer mechanisms, COHP calculations via LOBSTER software for H–Mg bond interaction evaluation [70]; ELF analysis through VESTA visualization system to characterize chemical bonding topology [71]; DOS calculations employing the VASPKIT package for electronic structure interpretation [72]; and Bader charge partitioning analysis to quantify interfacial charge redistribution during dehydrogenation processes. The Fermi level was aligned to zero in all analyses for consistent comparison of electronic features.

The ionicity index of the system was calculated by determining the average charge transfer, which serves as a parameter to evaluate the difficulty of dehydrogenation. The calculation formula is as follows:

$$\chi = \frac{|V_{\mathrm{val}} - Q_{\mathrm{Bader}}|}{V_{\mathrm{val}}} \tag{3}$$

Where V_{val} represents the number of valence electrons of the atom, Q_{Bader} represents the number of electrons actually assigned to the atom according to Bader charge analysis, and χ is the ionicity index used to evaluate the degree of electron redistribution of the atom. This formula reflects the proportion of charge transfer per valence electron in the structure. A value of χ close to 1 indicates that the atom behaves more like an ideal ionic species, while a lower value suggests that the electron distribution tends to be more covalent in nature.

3. Results and discussion

3.1. Surface structures and dehydrogenation of γ-MgH_2 in AIMD simulations

γ-MgH_2 crystallizes in the orthorhombic Pbcn space group. The conventional cell structure and lattice parameters of γ-MgH_2 are provided in Fig. S2 and Table S1 The initial bulk unit cell was modeled with lattice parameters of $a = 4.48$ Å, $b = 4.90$ Å, and $c = 5.39$ Å [73]. In this study, four representative low-index surfaces—(001), (100), (101), and (110)—were cleaved from the relaxed γ-MgH_2 bulk structure to investigate surface-dependent dehydrogenation behavior [74]. For each surface, a 2 × 2 supercell was constructed, and a vacuum layer of 15 Å was added along the z-direction to eliminate interactions between periodic images. The resulting H–Mg bond lengths range from 1.90 to 1.99 Å, which is consistent with previously reported experimental data [73]. This indicates that our computational results are reasonable. The constructed surface models are shown in Fig. 1, and detailed structural parameters are listed in Table S2.

Previous studies have shown that the dehydrogenation of MgH_2 is closely related to the presence of surface hydrogen atoms[54]. Therefore, to facilitate comparison, each surface was modeled with two types of terminations: configuration A corresponds to the hydrogen-rich surface, whereas configuration B represents the hydrogen-deficient one. This dual-configuration setup enables direct comparison to validate the reliability of the simulation results.

AIMD simulations were employed to monitor the surface behavior and capture the dynamic evolution of atomic configurations, enabling subsequent analysis of the unique bonding characteristics of H–Mg at the electronic structure level. According to experimental observations, the dehydrogenation temperature of γ-MgH_2 is approximately 100 °C [46]. Therefore, to reflect experimental conditions and ensure a balance between physical relevance and computational efficiency, the target temperature for the simulations was set to 373 K, which allows effective observation of dehydrogenation behavior within feasible simulation timescales.

The results indicate that dehydrogenation occurs on the (001)-A, (100)-A, (101)-A, and (110)-A surfaces. This further confirms the validity of our computational approach. The corresponding RDFs are shown in Fig. 2a–d. A distinct peak appears at approximately 0.75 Å in configuration A (highlighted in blue), which closely matches the H–H distance $d_{(\mathrm{H–H})}$ in molecular hydrogen and serves as direct evidence for the occurrence of dehydrogenation and the formation of H_2. The RMSD analysis of the dehydrogenated configuration is shown in Fig. 2e, while that of the non-dehydrogenated model is displayed in Fig. 2f. The final results of the AIMD simulations are shown in Fig. S3, all maintaining structurally stable configurations. Notably, the RMSD values for configuration A (with surface hydrogen) are consistently higher than those of configuration B (without surface hydrogen). For each surface, larger RMSD values show strong correlation with the occurrence of dehydrogenation, supporting the observed dynamic behavior.

However, the underlying reason for the exceptional dehydrogenation performance of γ-MgH_2 remains unclear. Therefore, it is necessary to investigate the unique characteristics of H–Mg bonds in γ-MgH_2 at the electronic structure level to uncover the fundamental mechanism behind its superior dehydrogenation behavior.

3.2. Insights into electronic structure and bonding mechanisms

AIMD simulation results indicate that γ-MgH_2 undergoes dehydrogenation at 373 K, demonstrating excellent dehydrogenation performance. To further understand the H–Mg interactions and bonding mechanisms in γ-MgH_2, COHP analyses were first conducted on all surface models to evaluate the bonding and antibonding contributions at various energy levels.

The -COHP curves of H–Mg bonds are shown in Fig. 3a-d. In these plots, the regions above the Fermi level represent antibonding states, while those below the Fermi level correspond to bonding states. A larger contribution from bonding states generally indicates greater structural stability. The computational results show that the configuration exhibiting dehydrogenation (configuration A) presents a noticeable occupation of antibonding orbitals below the Fermi level compared to the non-dehydrogenated configuration (configuration B). For comparison, we also calculated the -COHP of α-MgH_2, as shown in Fig. S4. The results reveal that states near the Fermi level are predominantly bonding in nature, with no significant antibonding occupation, indicating a stronger degree of electron delocalization and higher H–Mg bond strength in α-MgH_2.

The presence of significant antibonding states near the Fermi level in γ-MgH_2 suggests a weakened H–Mg interaction, facilitating easier dehydrogenation. In contrast, α-MgH_2 exhibits mainly bonding states below the Fermi level, indicating stronger H–Mg bonding and higher

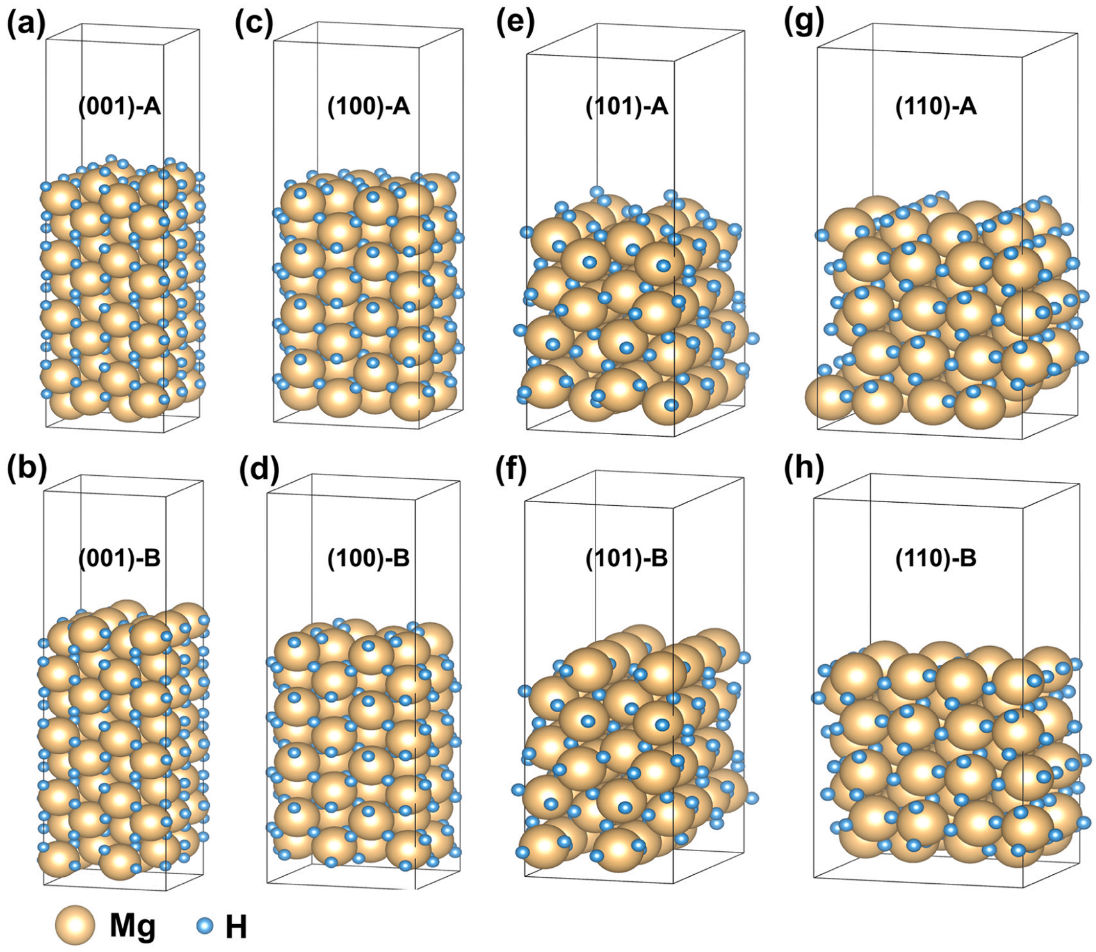

Fig. 1. (a–h) Initial structural models of the (001)-A, (001)-B, (100)-A, (100)-B, (101)-A, (101)-B, (110)-A, and (110)-B surfaces used in subsequent calculations. The light blue color represents H atoms, and the golden beige color represents Mg atoms.

thermal stability. Furthermore, the integrated crystal orbital Hamilton population (-ICOHP) values were calculated to quantify the bond strength between Mg and H atoms. According to the study by Li et al., the average -ICOHP value of the strongest H–Mg bonds associated with reactive surface H atoms provides an effective descriptor for dehydrogenation barriers[75]. Guided by this insight, we analyzed the corresponding surface H atoms in our initial configurations that meet this criterion. The integrated -ICOHP values were calculated and are summarized in Table 1 to support our conclusions, while the initial bonding data are provided in Table S3. However, we found that the calculated ICOHP values alone are insufficient to effectively classify all the models. Therefore, additional electronic structure analyses are necessary to assist in developing reliable descriptors for evaluating the dehydrogenation capability of the models.

Based on the above analysis, we identified that the superior dehydrogenation behavior of γ-MgH_2 primarily originates from the facile removal of surface hydrogen atoms. To further investigate the electronic evolution during the dehydrogenation process, we analyzed the ELFs along the surface-normal z-direction. The ELF map for the dehydrogenated configuration A is shown in Fig. 4a-d, where red regions correspond to highly localized electrons, and blue regions indicate low electron density.

As seen from the ELF results, the areas surrounding hydrogen atoms in configuration A appear as red, symmetric circular shapes, suggesting a high degree of electron localization and weak bonding interactions. As shown in Fig. 4, the regions marked by white circles indicate that the H atoms exhibit weaker interactions with the surrounding Mg atoms in the ELF maps, as evidenced by the reduced degree of electron localization. This behavior is notably different compared to the surface without hydrogen. In contrast, the ELF of the non-dehydrogenated configuration B (Fig. S5) exhibits larger red areas with more delocalized electron characteristics, indicating stronger bonding and a greater ionic character of the H–Mg bond. Additionally, the ELF of α-MgH_2 also shows a considerable area of high electron localization (Fig. S6), which further underscores the distinct advantage of γ-MgH_2 in terms of dehydrogenation performance. It is important to note that the above conclusion is drawn solely from the ELF analysis. To achieve a more comprehensive and quantitative understanding of the bonding characteristics and the degree of ionicity, further investigation of the electronic structure is necessary.

The COHP analysis provides quantitative insight into the bonding strength of H–Mg interactions and reveals the contributions of bonding and antibonding orbitals. Additionally, ELF results suggest that the system is primarily stabilized through ionic interactions. However, COHP and ELF alone are insufficient to fully characterize the electronic structure. To obtain a more comprehensive understanding, DOS calculations were carried out. These include both total density of states (TDOS) and projected density of states (PDOS), allowing us to investigate the contributions of individual orbitals and their occupation near the Fermi level. The DOS results offer deeper insight into the nature of the H–Mg bonding and the electronic behavior responsible for the dehydrogenation performance of the material.

Firstly, as shown in Fig. 5, the TDOS of the H-rich configuration A (dehydrogenation) exhibits broad DOS peaks that are distributed farther from the Fermi level, indicating delocalized electronic states. Compared to the non-dehydrogenated configuration, the broader DOS peaks imply

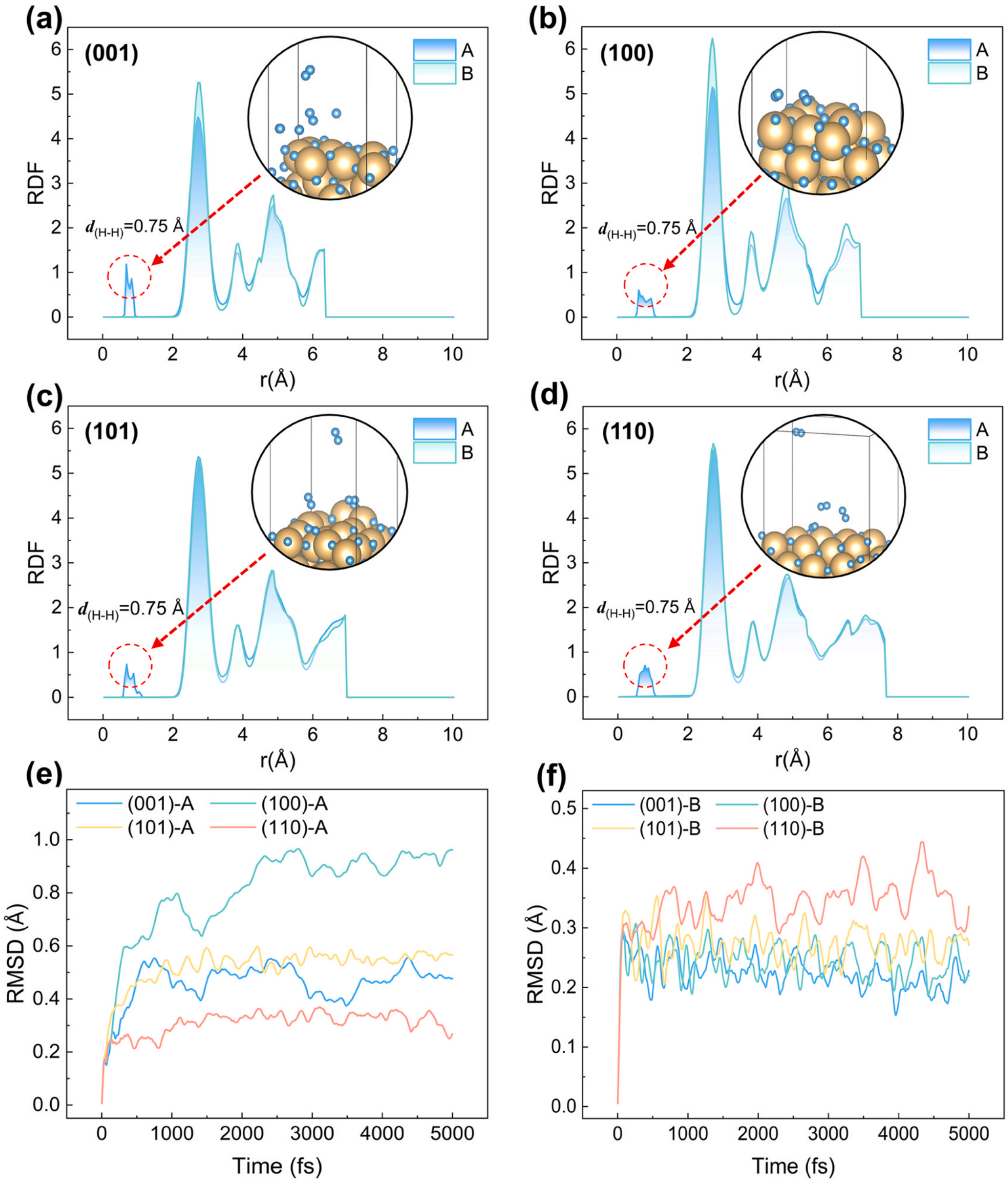

Fig. 2. (a-d) The RDFs and corresponding dehydrogenation behavior of γ-MgH_2 surfaces: (001), (100), (101), and (110), respectively. (e–f) RMSD values for the dehydrogenated and non-dehydrogenated configurations, respectively, indicating that all systems have reached structural equilibrium.

stronger orbital hybridization and a more pronounced covalent character in the bonding. Furthermore, the DOS profile of configuration A crosses the Fermi level, with no apparent band gap across the energy range, and a non-zero density of states at E_F. This suggests a metallic nature with good electronic conductivity and enhanced electron mobility, both of which are favorable for dehydrogenation behavior. In contrast, the DOS profile of the H-deficient configuration B, shown in Fig. S7, displays much sharper and narrower peaks located closer to the Fermi level, indicating stronger electron localization. A noticeable band gap is observed, with the DOS near Fermi level approaching zero, suggesting a more semiconducting nature and reduced electron mobility, which is less conducive to dehydrogenation.

To further resolve the orbital contributions from individual atoms, PDOS analysis was conducted. In the low-energy region (-6 ~ -2 eV), all H-*s* orbitals display pronounced peaks. Notably, the projected states of H-*s* in configuration A (Fig. 5a-d) appear less intense than those in the non-dehydrogenated configuration B, indicating that A is intrinsically weaker and thus more susceptible to dehydrogenation. In the overlapping region of H-*s* and Mg-*s* states, the bonding peak in configuration A is located at a lower energy compared to configuration B, indicating more stabilized bonding orbitals in the former. Additionally, the H-*s* states cross the Fermi level in configuration A, implying that the electrons of H atoms are no longer confined to deep valence states, which facilitates hydrogen desorption and H_2 formation. The prominent contribution of H-*s* near the Fermi level in γ-MgH_2 indicates enhanced hydrogen mobility and the potential for improved dehydrogenation behavior. In contrast, α-MgH_2 exhibits an electronic structure similar to that of γ-MgH_2 in configuration B, as evidenced by the DOS results presented in Fig. S8. A distinct band gap is present, with the DOS near the Fermi level approaching zero, indicating low electronic conductivity, which is unfavorable for the dehydrogenation process.

Furthermore, a pair of sharp peaks are observed on either side of the

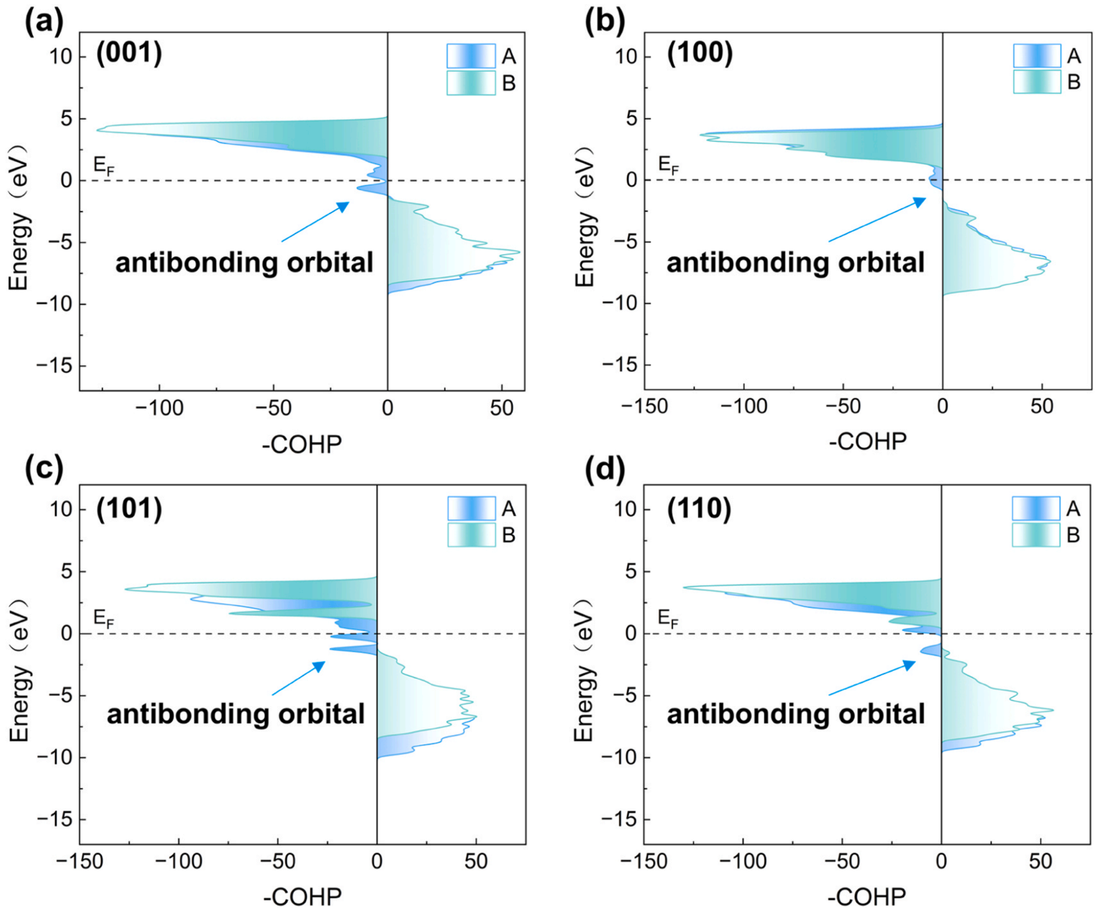

Fig. 3. (a–d) COHP analysis of the γ-MgH_2 surfaces (001), (100), (101), and (110), respectively. The dashed line indicates the Fermi level. The sky blue represents configuration A, and the mint green represents configuration B.

Table 1
ICOHP Values for γ and α-MgH_2 configurations.

Model	Configuration	-ICOHP (eV)
γ-MgH_2	(001)-A	0.35
	(001)-B	0.44
	(100)-A	0.49
	(100)-B	0.36
	(101)-A	0.38
	(101)-B	0.45
	(110)-A	0.45
	(110)-B	0.42
α-MgH_2	(101)	0.36
	(110)	0.96[54]

Fermi level, with a finite DOS between them, forming a pseudo-gap. A broader pseudo-gap is typically associated with weaker ionic bonding character and a lower ionicity index, both of which correlate with an increased tendency for dehydrogenation. According to the DOS analysis, γ-MgH_2 exhibits a relatively high electronic density of states near the Fermi level, which suggests enhanced electrical conductivity and elevated chemical reactivity—both favorable characteristics for efficient dehydrogenation.

Based on the above findings, it is evident that the electronic structure of H–Mg bonds is closely correlated with the material's dehydrogenation ability. To further elucidate the H–Mg interaction, Bader charge analysis was performed to quantify the charge transfer and evaluate the degree of ionicity within the system. The ionicity calculation data for each model are provided in Table S4. The ionicity indices of γ-MgH_2 models are illustrated in Fig. 6a, where configuration A corresponds to the dehydrogenated model and configuration B represents the non-dehydrogenated state. It is clearly observed that the blue bars (configuration A) exhibit lower ionicity indices compared to the light green bars (configuration B), suggesting that a lower ionicity index is beneficial for dehydrogenation in γ-MgH_2.

Subsequently, we performed similar Bader charge analyses for the (101) and (110) surfaces of α-MgH_2, and the corresponding ionicity indices are presented in Fig. 6b. The results show that the ionicity indices for both models—with and without surface hydrogen—are comparable, and neither configuration exhibits noticeable dehydrogenation behavior. Through statistical evaluation of the charge transfer and ionicity across different surface models, we found that when the ionicity index is lower than 0.77, the H–Mg bond strength becomes sufficiently weakened, enabling γ-MgH_2 to undergo dehydrogenation at relatively low temperatures (373 K). This newly identified criterion provides a compelling explanation, at the electronic structure level, for the superior dehydrogenation performance of γ-MgH_2.

Based on the above research, the main findings are summarized in the schematic mechanism diagram shown in Fig. 7. The top and bottom arrows indicate the decreasing trends of dehydrogenation temperature and ionicity index, respectively. The left side of the diagram corresponds to the α-MgH_2 phase where ELF reveals strong H–Mg bonding, a high ionicity index and a higher dehydrogenation temperature. In contrast, the right side illustrates the γ-MgH_2 phase obtained through ball milling, which shows weaker H–Mg bond strength as indicated by ELF, along with a lower ionicity index and reduced dehydrogenation temperature.

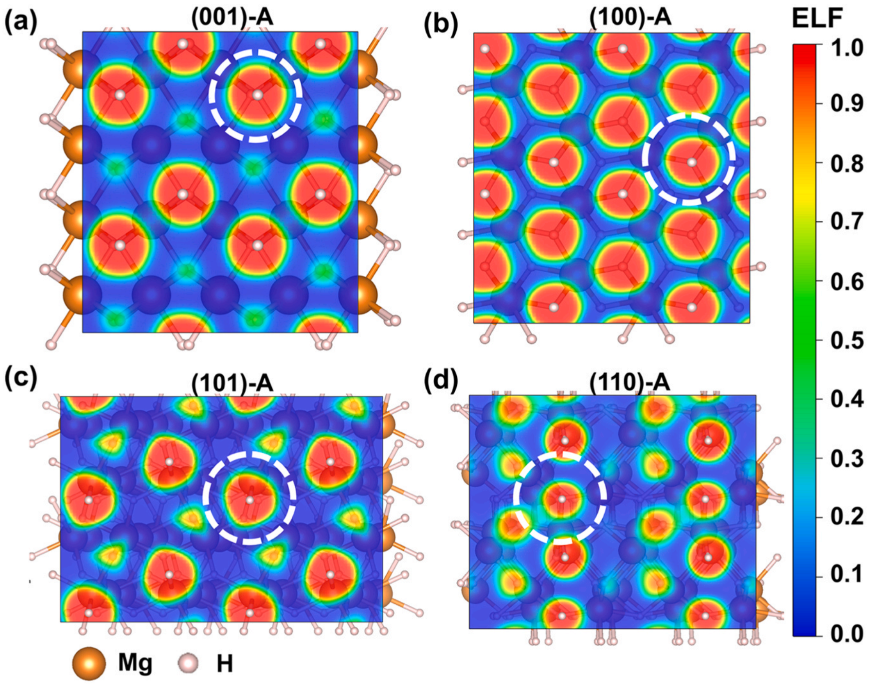

Fig. 4. (a-d) ELFs of the initial configurations (001)-A, (100)-A, (101)-A, and (110)-A, respectively. An ELF value of 1 indicates a fully localized state, 0.5 corresponds to a uniform electron gas, and 0 represents a fully delocalized state.

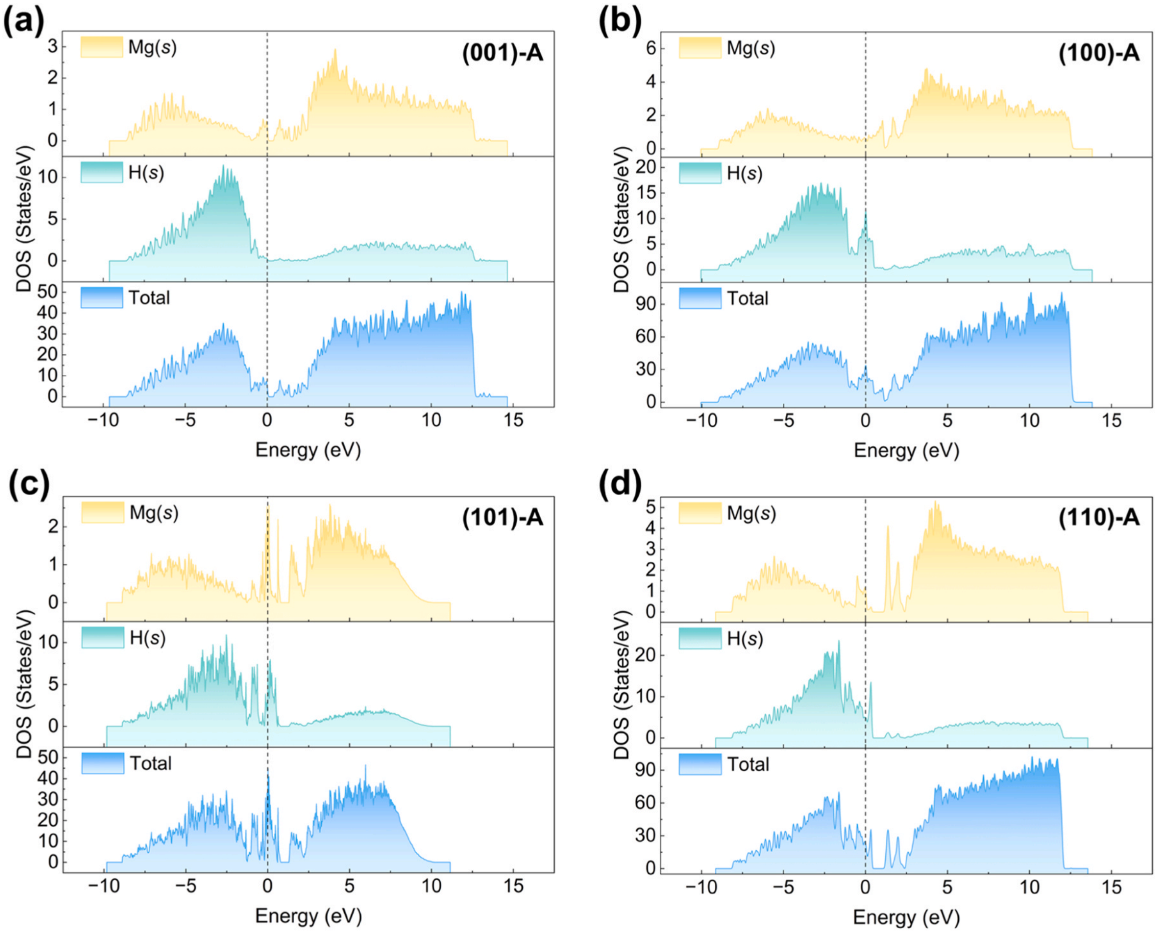

Fig. 5. DOS and PDOS for the initial configurations: (a) (001)-A, (b) (100)-A, (c) (101)-A, and (d) (110)-A.

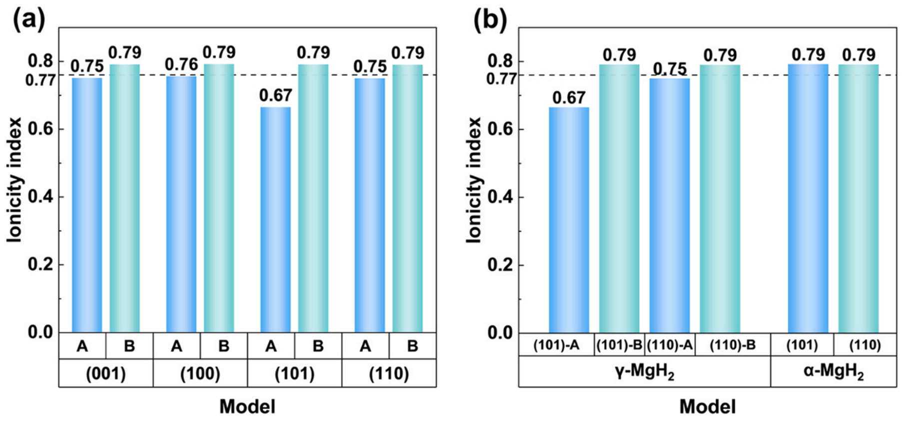

Fig. 6. (a) Distribution of ionicity indices for various surface configurations of γ-MgH_2; (b) Comparison of the ionicity index distributions between the (101) and (110) surfaces of γ-MgH_2 and α-MgH_2. The dashed line at 0.77 represents the threshold ionicity index distinguishing whether dehydrogenation occurs.

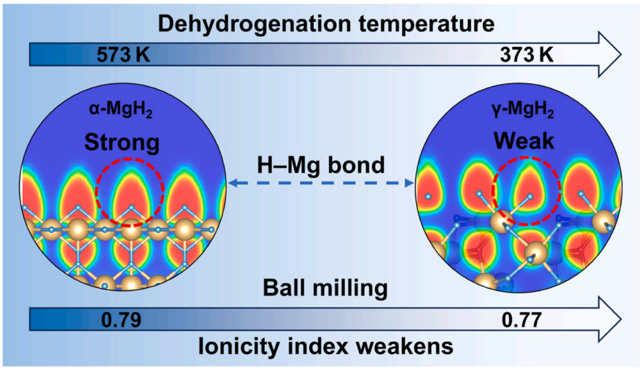

Fig. 7. Schematic representation of the mechanism by which ball milling weakens the H–Mg bond and promotes dehydrogenation.

4. Conclusion

In this study, we employed DFT-based electronic structure analysis to investigate the origin of the superior dehydrogenation performance of γ-MgH_2. The H–Mg bonds in MgH_2 are not purely ionic but possess a certain degree of covalency. COHP, ELF, and DOS analyses were used to evaluate the bonding characteristics, while the ionicity index derived from Bader charge analysis was applied to quantify the ionic bond strength. COHP analysis revealed significant anti-bonding states below the Fermi level in γ-MgH_2, indicating weaker H–Mg bonds compared to those in α-MgH_2. ELF and DOS results further confirmed reduced electron localization and enhanced hydrogen mobility in the γ-MgH_2. Bader analysis showed a markedly lower ionicity index in γ-MgH_2, especially at the surface, correlating with weaker ionic bonding. Notably, when this index drops below 0.77, spontaneous dehydrogenation occurs near 100 °C. Overall, by integrating DFT calculations with comprehensive electronic structure analysis, this work provides a microscopic explanation for the enhanced dehydrogenation behavior observed in mechanically activated MgH_2, such as through ball milling. These findings offer valuable engineering insights into how mechanical and structural modifications can effectively tune bonding characteristics in ionic hydrides like MgH_2, thereby improving hydrogen release kinetics and broadening their applicability in practical hydrogen storage systems.

CRediT authorship contribution statement

Xinyuan Liu: Software, Investigation. **Shuai Dong:** Writing – review & editing, Supervision. **Zhuoran Xu:** Validation, Investigation. **Tongao Yao:** Visualization, Formal analysis. **Wenfeng Fu:** Writing – review & editing, Writing – original draft, Validation, Supervision, Investigation, Formal analysis, Conceptualization. **Zhengyang Gao:** Supervision, Software. **Weijie Yang:** Writing – review & editing, Supervision, Resources, Project administration, Methodology, Funding acquisition, Conceptualization. **Man Shu:** Writing – original draft, Validation, Investigation, Data curation. **Yuxuan Liu:** Investigation, Data curation. **Jien Shi:** Validation, Investigation, Data curation.

Declaration of Generative AI and AI-assisted technologies in the writing process

During the preparation of this work, the authors used ChatGPT in order to improve language expression and check grammar. After using this tool, the authors reviewed and edited the content as needed and take full responsibility for the content of the publication.

Declaration of Competing Interest

The authors declare that they have no known competing financial interests or personal relationships that could have appeared to influence the work reported in this paper.

Acknowledgements

The authors gratefully acknowledge financial support for this work from the Natural Science Foundation of Hebei (Grant No. E2023502006) and Fundamental Research Fund for the Central Universities (2025MS131).

Appendix A. Supporting information

Supplementary data associated with this article can be found in the online version at doi:10.1016/j.jallcom.2025.182130.

References

[1] A.P. Zhao, S. Li, D. Xie, Y. Wang, Z. Li, P.J.-H. Hu, Q. Zhang, Hydrogen as the nexus of future sustainable transport and energy systems, Nat. Rev. Electr. Eng. (2025), https://doi.org/10.1038/s44287-025-00178-2.

[2] Materials for hydrogen mobile storage applications - IOPscience, (n.d.). ⟨https://iopscience.iop.org/article/10.1088/1755-1315/632/5/052087⟩ (accessed April 26, 2025).

[3] N. Ma, W. Zhao, W. Wang, X. Li, H. Zhou, Large scale of green hydrogen storage: Opportunities and challenges, Int. J. Hydrog. Energy 50 (2024) 379–396, https://doi.org/10.1016/j.ijhydene.2023.09.021.

[4] Y. Zhu, G.A. Keoleian, D.R. Cooper, The role of hydrogen in decarbonizing U.S. industry: a review, Renew. Sustain. Energy Rev. 214 (2025) 115392, https://doi.org/10.1016/j.rser.2025.115392.

[5] A. Albadwi, A. Elzein, A.A. Awad Bashir, S.B. Selçuklu, M.F. Kaya, Multi-criteria decision-making in hydrogen production, storage, and transportation: an overview,

Renew. Sustain. Energy Rev. 222 (2025) 115947, https://doi.org/10.1016/j.rser.2025.115947.

[6] K. Chen, M.Y. Lau, X. Luo, J. Huang, L. Ouyang, X.-S. Yang, Research progress in solid-state hydrogen storage alloys: a review, J. Mater. Sci. Technol. (2025) S1005030225006504, https://doi.org/10.1016/j.jmst.2025.05.037.

[7] M. Altaf, U.B. Demirci, A.K. Haldar, Review of solid-state hydrogen storage: materials categorisation, recent developments, challenges and industrial perspectives, Energy Rep. 13 (2025) 5746–5772, https://doi.org/10.1016/j.egyr.2025.05.034.

[8] H. Wang, J. Li, X. Wei, Y. Zheng, S. Yang, Y. Lu, Z. Ding, Q. Luo, Q. Li, F. Pan, Thermodynamic and kinetic regulation for mg-based hydrogen storage materials: Challenges, strategies, and perspectives, Adv. Funct. Mater. 34 (2024) 2406639, https://doi.org/10.1002/adfm.202406639.

[9] X. Wang, T. Cheng, H. Hong, H. Guo, X. Lin, X. Yang, B. Nie, Z. Hu, J. Zou, Challenges and opportunities in hydrogen storage and transportation: a comprehensive review, Renew. Sustain. Energy Rev. 219 (2025) 115881, https://doi.org/10.1016/j.rser.2025.115881.

[10] Y. Xu, Y. Zhou, Y. Li, Y. Hao, P. Wu, Z. Ding, Magnesium-based hydrogen storage alloys: advances, strategies, and future outlook for clean energy applications, Molecules 29 (2024) 2525, https://doi.org/10.3390/molecules29112525.

[11] C. Liang, Z. Wang, M. Zhang, C. Ma, Enhanced hydrogen storage property of MgH_2 caused by a $BaCrO_4$ nanocatalyst, RSC Adv. 14 (2024) 23930–23942, https://doi.org/10.1039/D4RA03460K.

[12] G. Xia, Y. Tan, X. Chen, D. Sun, Z. Guo, H. Liu, L. Ouyang, M. Zhu, X. Yu, Monodisperse magnesium hydride nanoparticles uniformly self-assembled on graphene, Adv. Mater. 27 (2015) 5981–5988, https://doi.org/10.1002/adma.201502005.

[13] S. Dong, C. Li, E. Lv, J. Wang, H. Liu, Z. Gao, W. Xiong, Z. Ding, W. Yang, H. Li, MgH_2 /single-atom heterojunctions: effective hydrogen storage materials with facile dehydrogenation, J. Mater. Chem. A 10 (2022) 19839–19851, https://doi.org/10.1039/D2TA02111K.

[14] S. Dong, H. Liu, X. Liu, C. Li, Z. Gao, B. Liu, W. Yang, Y. Wu, Facile dehydrogenation of MgH_2 enabled by γ-graphyne based single-atom catalyst, J. Energy Storage 74 (2023) 109484, https://doi.org/10.1016/j.est.2023.109484.

[15] L. Dan, H. Wang, X. Yang, J. Liu, L. Ouyang, M. Zhu, Low-temperature solid-state hydrogen storage via efficiently catalyzed MgH_2, Renew. Energy 231 (2024) 121009, https://doi.org/10.1016/j.renene.2024.121009.

[16] R. Kesarwani, A. Bhatnagar, S.K. Verma, M.S.L. Hudson, M.A. Shaz, Enhancement in hydrogen sorption behaviour of MgH_2 catalyzed by graphene quantum dots, Int. J. Hydrog. Energy 67 (2024) 1026–1032, https://doi.org/10.1016/j.ijhydene.2024.01.160.

[17] C. Liu, Z. Yuan, X. Li, Y. Sun, T. Zhai, Z. Han, L. Zhang, T. Li, Review on improved hydrogen storage properties of MgH_2 by adding new catalyst, J. Energy Storage 97 (2024) 112786, https://doi.org/10.1016/j.est.2024.112786.

[18] Y. Wang, Y. Xia, E. Xu, C. Xiang, X. Qing, Z. Yang, F. Xu, L. Sun, Y.S. Chua, Y. Zou, Graphene oxide supported oxygen vacancy-rich Co_3O_4 and ni nanoparticle for boosting the hydrogen storage properties of MgH_2, J. Magnes. Alloy. (2025) S2213956724004122, https://doi.org/10.1016/j.jma.2024.12.015.

[19] X. Liu, X. Meng, T. Zhong, Y. Wang, F. Wu, H. Liu, H. Li, L. Zhang, Polymeric carbon nitride supported single-phase Ni with exceptional catalytic effect on MgH2 for hydrogen storage, J. Alloy. Compd. 1032 (2025) 181259, https://doi.org/10.1016/j.jallcom.2025.181259.

[20] K. Iyakutti, R.P. Reji, K. Ajaijawahar, A. Karthigeyan, Y. Kawazoe, Exploring hydrogen storage properties of graphene-MgH_2 systems: a combined computational and experimental study, Int. J. Hydrog. Energy 139 (2025) 740–752, https://doi.org/10.1016/j.ijhydene.2025.05.215.

[21] D. Zhou, D. Zhao, H. Sun, P. Sheng, X. Zhang, J. Li, S. Guo, Y. Zhang, Two-dimensional material MXene and its derivatives enhance the hydrogen storage properties of MgH_2: a review and summary, Int. J. Hydrog. Energy 71 (2024) 279–297, https://doi.org/10.1016/j.ijhydene.2024.05.227.

[22] Y. Liu, H. Du, X. Zhang, Y. Yang, M. Gao, H. Pan, Superior catalytic activity derived from a two-dimensional Ti_3 C_2 precursor towards the hydrogen storage reaction of magnesium hydride, Chem. Commun. 52 (2016) 705–708, https://doi.org/10.1039/C5CC08801A.

[23] K. Nie, J. Li, H. Lu, R. Zhang, Y. Chen, F. Pan, Enhanced hydrogen storage properties of MgH_2 with alkalized Nb_2CT MXene: the role of enlarged interlayer spacing and optimized surface, Sep. Purif. Technol. 354 (2025) 129069, https://doi.org/10.1016/j.seppur.2024.129069.

[24] X. Zhang, Y. Sun, S. Ju, J. Ye, X. Hu, W. Chen, L. Yao, G. Xia, F. Fang, D. Sun, X. Yu, Solar-driven reversible hydrogen storage, Adv. Mater. 35 (2023) 2206946, https://doi.org/10.1002/adma.202206946.

[25] X. Zhang, S. Ju, C. Li, J. Hao, Y. Sun, X. Hu, W. Chen, J. Chen, L. He, G. Xia, F. Fang, D. Sun, X. Yu, Atomic reconstruction for realizing stable solar-driven reversible hydrogen storage of magnesium hydride, Nat. Commun. 15 (2024) 2815, https://doi.org/10.1038/s41467-024-47077-y.

[26] X. Hu, X. Chen, X. Zhang, Y. Meng, G. Xia, X. Yu, D. Sun, F. Fang, In situ construction of interface with photothermal and mutual catalytic effect for efficient solar-driven reversible hydrogen storage of MgH_2, Adv. Sci. 11 (2024) 2400274, https://doi.org/10.1002/advs.202400274.

[27] J. Zhang, W. Wang, X. Chen, J. Jin, X. Yan, J. Huang, Single-atom ni supported on TiO_2 for catalyzing hydrogen storage in MgH_2, J. Am. Chem. Soc. 146 (2024) 10432–10442, https://doi.org/10.1021/jacs.3c13970.

[28] H. Guan, J. Liu, Q. Li, Y. Lu, F. Pan, Chemically stable TMO @Ti-MgO (TM = Mn and Cu) catalyst enhanced de/hydrogenation kinetics of mg/MgH_2, J. Magnes. Alloy. (2025) S2213956725000957, https://doi.org/10.1016/j.jma.2025.02.032.

[29] Y. Jiang, Y. Sun, Y. Liu, M. Yue, Y. Cao, Q. Yuan, Y. Wang, Solar-driven reversible hydrogen storage in metal oxides-catalyzed MgH2, Int. J. Hydrog. Energy 149 (2025) 150101, https://doi.org/10.1016/j.ijhydene.2025.150101.

[30] Y. Liu, K. Zhong, K. Luo, M. Gao, H. Pan, Q. Wang, Size-dependent kinetic enhancement in hydrogen absorption and desorption of the Li−Mg−N−H system, J. Am. Chem. Soc. 131 (2009) 1862–1870, https://doi.org/10.1021/ja806565t.

[31] X. Zhang, Y. Liu, Z. Ren, X. Zhang, J. Hu, Z. Huang, Y. Lu, M. Gao, H. Pan, Realizing 6.7 wt% reversible storage of hydrogen at ambient temperature with non-confined ultrafine magnesium hydrides, Energy Environ. Sci. 14 (2021) 2302–2313, https://doi.org/10.1039/D0EE03160G.

[32] Y. Pang, Y. Liu, M. Gao, L. Ouyang, J. Liu, H. Wang, M. Zhu, H. Pan, A mechanical-force-driven physical vapour deposition approach to fabricating complex hydride nanostructures, Nat. Commun. 5 (2014) 3519, https://doi.org/10.1038/ncomms4519.

[33] H. Pan, Y. Liu, M. Gao, Y. Zhu, Y. Lei, Q. Wang, An investigation on the structural and electrochemical properties of $La_{0.7}Mg_{0.3}(Ni_{0.85}Co_{0.15})x$ (x=3.15–3.80) hydrogen storage electrode alloys, J. Alloy. Compd. 351 (2003) 228–234, https://doi.org/10.1016/S0925-8388(02)01045-9.

[34] J. Wo, W. Yang, Fullerene nano-confinement enables ultra-low dehydrogenation temperature of MgH_2: A DFT-based theoretical prediction, Int. J. Hydrog. Energy 146 (2025) 149987, https://doi.org/10.1016/j.ijhydene.2025.06.177.

[35] L. Fang, C. Liu, Y. Feng, Z. Gao, S. Chen, M. Huang, H. Ge, L. Huang, Z. Gao, W. Yang, Size-dependent nanoconfinement effects in magnesium hydride, Int. J. Hydrog. Energy 96 (2024) 783–793, https://doi.org/10.1016/j.ijhydene.2024.11.233.

[36] Q. Meng, Y. Huang, J. Ye, G. Xia, G. Wang, L. Dong, Z. Yang, X. Yu, Electrospun carbon nanofibers with in-situ encapsulated ni nanoparticles as catalyst for enhanced hydrogen storage of MgH2, J. Alloy. Compd. 851 (2021) 156874, https://doi.org/10.1016/j.jallcom.2020.156874.

[37] X. Zhao, S. Wu, X. Chen, L. Liu, Y. Deng, L. Zhou, X. Cai, Mechanism of hydrogenation and dehydrogenation in mg/Cu_9Al_4 @mg and MgH_2/Cu_9Al_4 @MgH_2: a DFT and experimental investigation, J. Alloy. Compd. 978 (2024) 173542, https://doi.org/10.1016/j.jallcom.2024.173542.

[38] W. Luo, C. Xu, K. Wang, Y. Ma, Z. Wu, C. Zhao, Y. He, S. Sun, H. Leng, C. Sun, Q. Li, C. Wu, Multivalent Ti/Nb catalysts with oxygen vacancies: bridging electron transfer pathways to enhance MgH2 hydrogen desorption property, J. Alloy. Compd. 1031 (2025) 181070, https://doi.org/10.1016/j.jallcom.2025.181070.

[39] Y. Chen, X. Li, B. Sun, G. Zhang, S. Ni, C. Li, Effect of NiFe-LDH/FeO(OH) derivatives on the hydrogen storage properties of MgH2, Int. J. Hydrog. Energy 121 (2025) 326–336, https://doi.org/10.1016/j.ijhydene.2025.03.367.

[40] S. Long, Y. Qin, H. Fu, J. Hu, H. Xue, Y. Chen, F. Pan, Hydrogen storage properties of MgH2 modified by efficient $Co_3V_2O_8$ catalyst, Sep. Purif. Technol. 341 (2024) 126901, https://doi.org/10.1016/j.seppur.2024.126901.

[41] W. Hu, J. Zang, Q. Wang, S. Xiao, J. Zhang, F. Fang, Z. Ma, D. Sun, Y. Song, Spring effect endowing P-doped Li_3 VO_4 with long-standing catalytic activity for tuning cycling stability of MgH_2, Adv. Energy Mater. 15 (2025) 2404650, https://doi.org/10.1002/aenm.202404650.

[42] L. Shen, Z. Li, Y. Lu, G. Wei, Q. Li, Y. Yang, F. Pan, Enhancing thermodynamic and kinetic properties of MgH_2 by addition of the $V_{80}Ti_8Cr_{12}$ alloy, J. Alloy. Compd. 1010 (2025) 177591, https://doi.org/10.1016/j.jallcom.2024.177591.

[43] G. Gao, Z. Yao, J. Gu, J. Xie, C. Li, M. Fan, X. Xiao, L. Chen, From lab to plant: Process design and scalability challenges in MgH_2 synthesis, Chem. Eng. J. 517 (2025) 164364, https://doi.org/10.1016/j.cej.2025.164364.

[44] A.D.M. Charles, A.N. Rider, S.A. Brown, C.H. Wang, The effect of high energy ball milling on terfenol-D, J. Alloy. Compd. 1010 (2025) 178030, https://doi.org/10.1016/j.jallcom.2024.178030.

[45] D. Zhao, X. Hou, Y. Ge, D. Sun, D. Li, C. Wang, X. Xie, P. Zhu, X. Ye, G. Suo, Y. Yang, Nanosizing enhancement of hydrogen storage performance and mechanism in mg-based materials: nano-substrate modulation, nano-catalyst construction, and nano-catalytic mechanisms, J. Energy Chem. 109 (2025) 609–636, https://doi.org/10.1016/j.jechem.2025.06.005.

[46] Z. Weng, I. Retita, Y.-S. Tseng, A.J. Berry, D.R. Scott, D. Leung, Y. Wang, S.L. I. Chan, γ-MgH2 induced by high pressure for low temperature dehydrogenation, Int. J. Hydrog. Energy 46 (2021) 5441–5448, https://doi.org/10.1016/j.ijhydene.2020.11.044.

[47] H. Simchi, A. Kaflou, A. Simchi, Structural characteristics and desorption properties of nanostructured MgH_2 synthesised by high energy mechanical milling, Powder Metall. 54 (2011) 480–483, https://doi.org/10.1179/003258909X12502872942372.

[48] Y. Wang, X. Chen, H. Zhang, G. Xia, D. Sun, X. Yu, Heterostructures built in metal hydrides for advanced hydrogen storage reversibility, Adv. Mater. 32 (2020) 2002647, https://doi.org/10.1002/adma.202002647.

[49] H.R. Gopidi, L. Vashist, O.I. Malyi, Unveiling defect physics in gapped metals: A theoretical investigation into defect formation and electronic structure interplay, J. Mater. Inf. 5 (2025), https://doi.org/10.20517/jmi.2024.41.

[50] B. Han, F. Li, Regulating the electrocatalytic performance for nitrogen reduction reaction by tuning the N contents in Fe_3 @N_x C_{20-x} ($x = 0$–4): A DFT exploration, J. Mater. Inf. 3 (2023), https://doi.org/10.20517/jmi.2023.32.

[51] X. Zhang, C. Li, J. Ye, X. Hu, W. Chen, F. Fang, D. Sun, Y. Liu, X. Yu, G. Xia, Light-enabled reversible hydrogen storage of borohydrides activated by photogenerated vacancies, J. Am. Chem. Soc. 147 (2025) 2786–2796, https://doi.org/10.1021/jacs.4c15744.

[52] Y.J. Kwak, M.Y. Song, K.-T. Lee, Synergistic effects of $NaAlH_4$, $LiBH_4$, and ni additives on the hydrogen storage performance of MgH_2, J. Alloy. Compd. 1032 (2025) 181138, https://doi.org/10.1016/j.jallcom.2025.181138.

[53] A.I. Bashir, M.H. Sahafi, S. Saeed, First-principles quantum insights into phonon dynamics and thermophysical potential of MgH_2 and MgH_2:Mo for enhanced thermoelectricity and hydrogen energy applications, Renew. Energy 247 (2025) 123008, https://doi.org/10.1016/j.renene.2025.123008.

[54] S. Dong, C. Li, J. Wang, H. Liu, Z. Ding, Z. Gao, W. Yang, W. Lv, L. Wei, Y. Wu, H. Li, The "burst effect" of hydrogen desorption in MgH_2 dehydrogenation, J. Mater. Chem. A 10 (2022) 22363–22372, https://doi.org/10.1039/D2TA06458H.

[55] J. Cai, Y. Jiang, T. Yao, X. Tang, Y. Liu, Z. Xu, X. Zhao, B. Zhang, Z. Gao, W. Yang, A demand-driven dynamic heating strategy for ultrafast and energy-efficient MgH_2 dehydrogenation utilizing the "burst effect, J. Energy Storage 130 (2025) 117495, https://doi.org/10.1016/j.est.2025.117495.

[56] J.M. Sander, L. Ismer, C.G. Van De Walle, Point-defect kinetics in α- and γ-MgH2, Int. J. Hydrog. Energy 41 (2016) 5688–5692, https://doi.org/10.1016/j.ijhydene.2016.01.156.

[57] J.A. Kammerer, X. Duan, F. Neubrech, R.R. Schröder, N. Liu, M. Pfannmöller, Stabilizing γ-MgH_2 at nanotwins in mechanically constrained nanoparticles, Adv. Mater. 33 (2021) 2008259, https://doi.org/10.1002/adma.202008259.

[58] T. Kelkar, S. Pal, A computational study of electronic structure, thermodynamics and kinetics of hydrogen desorption from al- and si-doped α-, γ-, and β-MgH_2, J. Mater. Chem. 19 (2009) 4348, https://doi.org/10.1039/b901115c.

[59] W.-Y. Chen, J.-J. Tang, Z.-W. Lu, M.-X. Huang, L. Liu, C.-C. He, Y.-J. Zhao, Theoretical investigation of the surface orientation impact on the hydrogen vacancy formation of MgH2, Surf. Sci. 710 (2021) 121850, https://doi.org/10.1016/j.susc.2021.121850.

[60] J.H. Dai, Y. Song, R. Yang, Intrinsic mechanisms on enhancement of hydrogen desorption from MgH_2 by (001) surface doping, Int. J. Hydrog. Energy 36 (2011) 12939–12949, https://doi.org/10.1016/j.ijhydene.2011.07.062.

[61] V.L. Deringer, A.L. Tchougréeff, R. Dronskowski, Crystal orbital hamilton population (COHP) analysis as projected from plane-wave basis sets, J. Phys. Chem. A 115 (2011) 5461–5466, https://doi.org/10.1021/jp202489s.

[62] R. Dronskowski, P.E. Bloechl, Crystal orbital hamilton populations (COHP): Energy-resolved visualization of chemical bonding in solids based on density-functional calculations, J. Phys. Chem. 97 (1993) 8617–8624, https://doi.org/10.1021/j100135a014.

[63] G. Kresse, D. Joubert, From ultrasoft pseudopotentials to the projector augmented-wave method, Phys. Rev. B 59 (1999) 1758–1775, https://doi.org/10.1103/PhysRevB.59.1758.

[64] J.P. Perdew, K. Burke, M. Ernzerhof, Generalized gradient approximation made simple, Phys. Rev. Lett. 77 (1996) 3865–3868, https://doi.org/10.1103/PhysRevLett.77.3865.

[65] R. Chapai, P.V.S. Reddy, L. Xing, D.E. Graf, A.B. Karki, T.-R. Chang, R. Jin, Evidence for unconventional superconductivity and nontrivial topology in PdTe, Sci. Rep. 13 (2023) 6824, https://doi.org/10.1038/s41598-023-33237-5.

[66] H. Zheng, H. Li, W. Song, Z. Zhao, G. Henkelman, Calculations of hydrogen associative desorption on mono- and bimetallic catalysts, J. Phys. Chem. C. 125 (2021) 12028–12037, https://doi.org/10.1021/acs.jpcc.1c03466.

[67] J. Wellendorff, T.L. Silbaugh, D. Garcia-Pintos, J.K. Nørskov, T. Bligaard, F. Studt, C.T. Campbell, A benchmark database for adsorption bond energies to transition metal surfaces and comparison to selected DFT functionals, Surf. Sci. 640 (2015) 36–44, https://doi.org/10.1016/j.susc.2015.03.023.

[68] S. Grimme, J. Antony, S. Ehrlich, H. Krieg, A consistent and accurate *ab initio* parametrization of density functional dispersion correction (DFT-D) for the 94 elements H-pu, J. Chem. Phys. 132 (2010) 154104, https://doi.org/10.1063/1.3382344.

[69] W. Humphrey, A. Dalke, K. Schulten, VMD: Visual molecular dynamics, J. Mol. Graph. 14 (1996) 33–38, https://doi.org/10.1016/0263-7855(96)00018-5.

[70] S. Maintz, V.L. Deringer, A.L. Tchougréeff, R. Dronskowski, LOBSTER: A tool to extract chemical bonding from plane-wave based DFT, J. Comput. Chem. 37 (2016) 1030–1035, https://doi.org/10.1002/jcc.24300.

[71] K. Momma, F. Izumi, *VESTA 3* for three-dimensional visualization of crystal, volumetric and morphology data, J. Appl. Crystallogr 44 (2011) 1272–1276, https://doi.org/10.1107/S0021889811038970.

[72] V. Wang, N. Xu, J.-C. Liu, G. Tang, W.-T. Geng, VASPKIT: a user-friendly interface facilitating high-throughput computing and analysis using VASP code, Comput. Phys. Commun. 267 (2021) 108033, https://doi.org/10.1016/j.cpc.2021.108033.

[73] M. Bortz, B. Bertheville, G. Böttger, K. Yvon, Structure of the high pressure phase γ-MgH2 by neutron powder diffraction, J. Alloy. Compd. 287 (1999) L4–L6, https://doi.org/10.1016/S0925-8388(99)00028-6.

[74] R.A. Varin, T. Czujko, Z. Wronski, Particle size, grain size and γ-MgH_2 effects on the desorption properties of nanocrystalline commercial magnesium hydride processed by controlled mechanical milling, Nanotechnology 17 (2006) 3856–3865, https://doi.org/10.1088/0957-4484/17/15/041.

[75] C. Li, W. Yang, H. Liu, X. Liu, X. Xing, Z. Gao, S. Dong, H. Li, Picturing the gap between the performance and US-DOE's hydrogen storage target: a data-driven model for MgH $_2$ dehydrogenation, Angew. Chem. Int Ed. 63 (2024) e202320151, https://doi.org/10.1002/anie.202320151.